Investigation of target erosion profiles sputter-eroded by a low-energy broad ion beam

Wjatscheslaw Sakiew, Eileen Klocke and Detlev Ristau

ARTICLES YOU MAY BE INTERESTED IN

READ NOW!

AIP Advances

Photonics and Optics Collection

Investigation of target erosion profiles sputter-eroded by a low-energy broad ion beam

View Online   Export Citation   CrossMark

Wjatscheslaw Sakiew,[1,a)] (iD) Eileen Klocke,[1] and Detlev Ristau[2] (iD)

AFFILIATIONS

[1] Cutting Edge Coatings GmbH, Garbsener Landstrasse 10, 30419 Hannover, Germany
[2] Laser Zentrum Hannover e.V., Hollerithallee 8, 30419 Hannover, Germany
[3] Cluster of Excellence PhoenixD (Photonics, Optics, and Engineering – Innovation Across Disciplines), Leibniz University Hannover, Hannover, Germany

[a)] Author to whom correspondence should be addressed: w.sakiew@gmail.com

ABSTRACT

The demand for ion beam sputtering (IBS) coated substrates is growing. In order to find new fields of application for IBS coating technology, it is necessary to understand in detail the distributions of the involved particles in an industrial-scale reactive coating process. In pursuit of this goal, in the present investigation, profiles sputter-eroded from tantalum, silicon, and silicon dioxide targets by a low-energy broad ion beam (ion energy $\leq$ 1.9 keV, ion source RIM-20) are measured with a mechanical profilometer and compared. To approximate the discrete and two-dimensional erosion data accurately, an empirical function is developed. For an applied target tilt angle of $55°$, the results indicate that the actual angle-dependent ion–solid interaction mechanisms at the atomic level have a rather subordinate role in the macroscopic surface modification of the target in terms of the qualitative distribution of the erosion profile. The applied process geometry seems to have a much larger impact. Furthermore, in the case of silicon, a linear erosion rate as a function of erosion time is observed. Thus, the form of the broad erosion profile does not seem to have a measurable effect on the erosion rate.

I. INTRODUCTION

Ion beam sputter deposition (IBSD) is a well-established coating technology in optical thin film production facilities. The properties, applications, and achievable quality parameters have been well-documented in open literature.[1–3] Mirror coatings for gravitational wave detectors[4] and ring laser gyroscopes for inertial rotation measurements[5] are prominent scientific applications. A key element in ion beam sputtering (IBS) is the ion beam—predominantly a composition of primary particles, with which target atoms (secondary particles) are sputtered from a target surface. The removal of atoms by energetic ions is equivalent to an erosion process.

Over the past few decades, IBSD has been continuously improved,[6] new concepts have been implemented,[7–9] and systematic investigations of the underlying physical mechanisms have been carried out.[10,11] In contrast, the productivity parameters and economic factors involved have not received much attention. It is only in the last few years that a certain trend toward large-area optical coatings in the field of IBSD has been observed. The achievable uniform

deposition areas are still smaller than 1 m in diameter.[12,13] However, it is to be expected that larger coatings with an IBSD quality level will be required for future applications, e.g., meter-sized optical coatings for astronomy and space applications or meter-sized high-power laser optics for large optical systems.[14]

To open up new fields of application, there is a need to understand in detail the distributions of primary and secondary particles in an industrial-scale IBSD process. The approximation of the sputtering geometry by a single common point source as the point of origin of all sputtered particles is insufficient in this context if a broad ion beam is applied.[12] More precisely, in order to develop an understanding of how particle fluxes of secondary particles are emitted qualitatively and quantitatively from the target, it is necessary to know how the primary particles impinging on the target surface are distributed. In relation to this, the investigation of erosion profiles, as has been done for magnetron sputtering (MS), ion beam figuring (IBF), and focused ion beam microscopy tools over the past few decades, provides valuable information about the distributions of the involved particles. Comparable investigations in the field of IBSD,

which apply a broad ion beam and a tilted target, are not known to the authors (in Ref. 15, the RIM-10 ion source is used, which erodes a substrate made of silicon at a normal angle of incidence). The present investigation is intended to present corresponding experimental data and to provide a basis for modeling the distribution of the primary particles on the target surface later.

In the field of MS, which is a coating technology competing with IBSD (e.g., Ref. 16), an erosion profile is often referred to as a racetrack, erosion groove, or depth profile. In the case of reactive MS, target poisoning according to Berg's model[17] or the RSD2013 model[18] is an important additional mechanism and is most probably also relevant to reactive IBSD. Recently published results[19] indicate an almost fully oxidized titanium target surface during IBS in the presence of an O_2 atmosphere. In addition to that, stronger target poisoning of titanium targets compared to tantalum targets was a conclusion of Ref. 20.

Basic differences between IBF, IBSD for scientific purposes (with a focus on ion–solid interaction mechanisms), and industrial-scale IBSD processes (with a focus on production) are as follows: (1) the open diameter D_{optic} of the applied ion optic (which corresponds to the initial size of an ion beam[21]) with which ions are extracted from a plasma and an ion beam is formed, (2) the extracted ion beam current I_{beam}, (3) the distance d_{target} between the ion optic and the target (the beam propagation length), and (4) the resulting distribution of ions on the target surface.

In IBF processes, a smaller beam diameter on the workpiece to be machined (after beam propagation) possesses stronger error correction ability.[22] It is preferable that the beam shape and the resulting removal function on the workpiece are Gaussian. To meet these criteria, ion optics with D_{optic} in the range of 10–50 mm are applied.[22,23] In addition to that, diaphragms with diameters down to 0.5 mm are mounted between the ion source and the workpiece for beam shaping.[22,24] Literature values for I_{beam} vary in the range of 1–40 mA, and values for d_{target} of up to ~80 mm can be found.

For scientific investigations of ion–solid interaction mechanisms, the situation is quite similar. A small ion optic in combination with a corresponding short distance d_{target} ensures that only a small area on the target is sputtered by the primary particles (compared to the distance of secondary particle observation), which enables the consideration of a sputtering point source. Furthermore, a shorter ion propagation length reduces the number of ions that do not reach the target as a consequence of a finite mean free path. In Refs. 25–28, for instance, the following configurations were chosen for investigations of IBS and IBSD: D_{optic} = 16 mm, I_{beam} in the range of 6–10 mA, and d_{target} = 150 mm.

For industrial-scale IBSD processes, the situation is different. In order to meet the productivity demands of the optical thin film industry, higher beam currents are required to produce a certain quantity of secondary particles per unit time. From practical experience, I_{beam} varies in the range of 200–500 mA for high-quality thin film production. For beam currents in this range and above, it is necessary to distribute the ions over an appropriate target surface size. Otherwise, the target material is consumed too fast and the manufacturing of complex filters with corresponding long process durations becomes unfeasible. So far, the technically best solution is to apply a broad ion beam produced by a large multi-aperture extraction system. D_{optic} is usually larger than 100 mm, and the market even offers ion optics for IBSD with up to

D_{optic} = 220 mm. A higher beam current and, thus, a higher coating rate are the main benefits of a large ion optic. It is advantageous to adjust d_{target} to be as large as possible to prevent fast degradation of the ion optic through particle fluxes originating from the target, although this can affect the productivity of an IBSD process significantly.[20] Thus, productivity values as well as economic factors depend on d_{target}. For instance, in the IBSD coating machines NAVIGATOR 1100 and NAVIGATOR 2100,[12,20] manufactured by Cutting Edge Coatings GmbH (CEC), the common setups have d_{target} > 350 mm. From practical experience, target distances in the range of 200–550 mm are used in IBSD for the production of optical thin films.

The focus of this work is to investigate target erosion profiles during low-energy (ion energy ≤ 1.9 keV, ion source RIM-20) reactive broad ion beam sputtering on a millimeter scale. Erosion profiles sputter-eroded from tantalum (Ta), silicon (Si), and silicon dioxide (SiO_2) targets are experimentally determined and compared with one another. Ta is chosen because it is one of the most common "high-index" materials used for IBSD processes in optical thin-film technology. Equally, Si and SiO_2 are the most commonly used "low-index" materials. All three target materials are preferred for the production of low-loss mirror coatings in the VIS and near-infrared (NIR) regions. Two different distances of d_{target} = 370 mm and d_{target} = 550 mm are examined.

II. EXPERIMENTAL METHOD

The sputter-erosion of the investigated Ta, Si, and SiO_2 targets was performed in CEC's NAVIGATOR 1100,[20] an industrial-scale IBS coating machine, with a sputter-up configuration of the main process components. The equipment is evacuated by a cryopump to a base pressure of 4×10^{-6} Pa in the high vacuum range. To generate a broad ion beam, NAVIGATOR 1100 is equipped with the inductively coupled radio-frequency (RF) type ion source RIM-20. The design is based on the RIT.[29,30] RIM-20 runs with a spherical shaped curve three-grid multi-aperture extraction system (accel-decel technique) made of titanium, with D_{optic} = 160 mm and a curvature radius R_{optic} = 400 mm. The ions are extracted from the plasma and accelerated by 847 beamlets distributed in a quasi-hexagonal pattern. All beamlets together make an ion optic transparency of 56.6%. Figure 1 shows the broad ion beam. To compensate for the space charge, a radio-frequency neutralizer (RFN) operates simultaneously with RIM-20 as a filament-less electron source (not shown in Fig. 1).

The sputter-erosion of the initially flat targets took place during several independent production processes of optical thin films and, thus, always in the presence of an O_2 atmosphere. To adjust the ion energy, only the beam voltage was varied (the accelerator grid voltage of −600 V and decelerator grid voltage of 0 V were not varied). The Si target was sputtered with a fixed set of parameters: 1.4 keV xenon (Xe) ions, I_{beam} = 200 mA, O_2 flow rate 90 SCCM, and working pressure in the range 5.3–8.5×10^{-2} Pa (depending on the position in the process chamber). The Ta target was sputtered under two sets of conditions: (1) with 1.8 keV argon (Ar) ions and with I_{beam} = 310 mA and (2) with 1.45 keV Xe ions and with I_{beam} = 230 mA. In both cases (1) and (2), the O_2 flow rate was set to 90 SCCM. For the sputtering of the SiO_2 target, 1.9 keV Ar ions and a 20 SCCM O_2 flow rate were selected. In all cases, an Ar flow rate
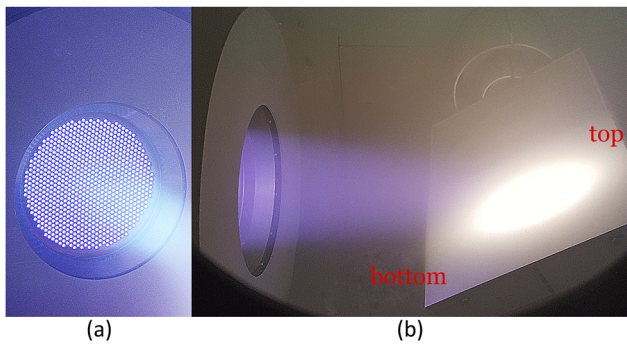
FIG. 1. IBSD process in CEC's industrial-scale coating machine NAVIGATOR 1100. (a) Front view of the operating multi-aperture ion optic of the ion source RIM-20 and (b) side view of the broad ion beam during the sputter-erosion of a target. The length of the target from bottom to top is 250 mm.

FIG. 2. A sputter-eroded Si target with dimensions $200 \times 250 \times 6$ mm^3, sputtered by a beam of 1.4 keV Xe ions, with $I_{beam} = 200$ mA, TTA = 55°, and $d_{target} = 370$ mm. (a) A top view and (b) an enlargement of the top view at $T = 135,092$ s and $z_{min} = -4.17$ mm. (c) An enlargement at $T = 76,058$ s and $z_{min} = -2.48$ mm. Circled numbers 1–4 and the fracture are explained in the main text.

of 20 SCCM or a Xe flow rate of 15 SCCM was used to operate RIM-20. It is important to note that regulation of the ion energy usually results in a variation of the beam profile.[30,31] The process parameters listed—ion species, ion energy, and beam current—are the result of process optimizations aimed at achieving specific process properties (lateral layer uniformity, coating rate) and layer quality parameters in thin film production.

In all processes, the targets were tilted at 55°. In IBSD, target tilt angles (TTAs) in the range of 45°–65° are usually used. At smaller angles, the particle flux of secondary particles increases in the backward direction toward the ion optic (degradation of the ion optic), and the sputtering yield decreases (reduction of productivity). With larger angles, the proportion of primary particles that fly past the target increases (reduction of productivity, adverse parasitic sputtering of process chamber parts behind the target). Additionally, at large angles of incidence, the sputtering yield drops rapidly (reduction of productivity). The target tilt angle is measured between the target surface normal and the symmetry axis $\vec{n}_{beam}$ of the ion beam. $\vec{n}_{beam}$ also corresponds to the direction of propagation of the broad ion beam and is hereinafter also referred to as the beam vector. In the cases of Ta and Si, the target distance—ion optic to the target surface—measured along $\vec{n}_{beam}$ was set to $d_{target} = 370$ mm (the corresponding setup is shown in Fig. 1). For the erosion of the SiO$_2$ target, a distance of $d_{target} = 550$ mm was applied. Thus, the dielectric target was positioned behind the geometric focal point of the ion optic ($d_{target} > R_{optic}$), while the Ta and Si targets were located before the geometrical focal point. The target holder was electrically grounded (with a contact resistance from target to ground <1 Ω) to eliminate potential electrical charging of the metallic targets.

To determine an erosion profile, the corresponding target was dismounted from the water-cooled target holder and its erosion was measured with a self-built mechanical profilometer. For each data record $z_i(x_i, y_i)$, the erosion depths z_i were measured with an accuracy of ±0.03 mm at up to 315 positions (x_i, y_i), almost evenly distributed over the relevant target area of 200×250 mm^2 [shown in detail in Fig. 3(a)]. The positioning accuracy of the profilometer amounts to 0.2 mm in the radial direction around each position (x_i, y_i). For describing the erosion processes, the values z_i are
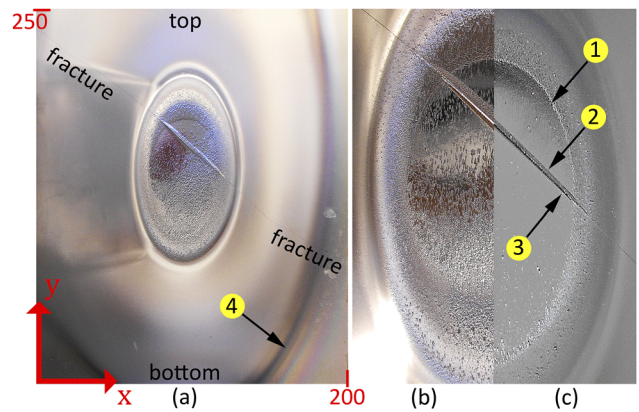
treated as negative values ($z = 0$ corresponds to the initial flat surface). x_i and y_i are measured in the chosen coordinate system of a target, as shown in Fig. 2(a). In the cases of Ta and Si, the target plate thickness amounts to 6 mm. The target plate thickness of the SiO$_2$ target amounts to 8 mm. In the case of Si, six measurements were performed to investigate the evolution of the erosion characteristics as a function of erosion time T. The Ta and SiO$_2$ targets were measured once. As described above, the erosion profile of Ta (Figs. 4 and 7) results from erosion processes with different ion beam parameters.

It is plausible to assume that the interaction process between an almost rotationally symmetric broad ion beam with a laterally inhomogeneous beam profile and a flat tilted target surface results in (1) a mirror-symmetric erosion profile and (2) irregular sputter conditions depending on the sputter position. In other words, it is assumed that the number of ions per unit area (and per unit time) and the angles of incidence of the ions are different for each point on the target surface (except for the corresponding symmetry points). Figures 2(a)–2(c) support both assumptions (1) and (2). In Figs. 2(a) and 2(b), the investigated Si target is shown after a total accumulated erosion time of $T = 135,092$ s (~37.5 h). A general observation is a quasi-elliptical-shaped and mirror-symmetric erosion zone (actually, this observation is irrespective of a specific target material, see also Fig. 7 in the Appendix). The maximum erosion depth is $z_{min} = -4.17$ mm (shown in detail in Fig. 3). At values $z_{min} \leq -6$ mm, the thickness of the target plate is exceeded, as mentioned above.

For comparison, Fig. 2(c) shows the same target after a shorter erosion time of $T = 76,058$ s (~21.2 h). Without generalizing, especially in the case of Si, two segments can be observed—a smooth inner segment (subjectively smoother than the initial surface) and a rough outer segment (subjectively rougher than the initial surface), separated by a more or less sharp edge [marked No. 1 in Fig. 2(c)]. In the course of sputter erosion, the inner segment reveals a rough spotty appearance as can be seen in Fig. 2(b). On the one hand, this irregular and dynamic structuring of a target surface could be assumed to be an expression of the position-dependent sputter
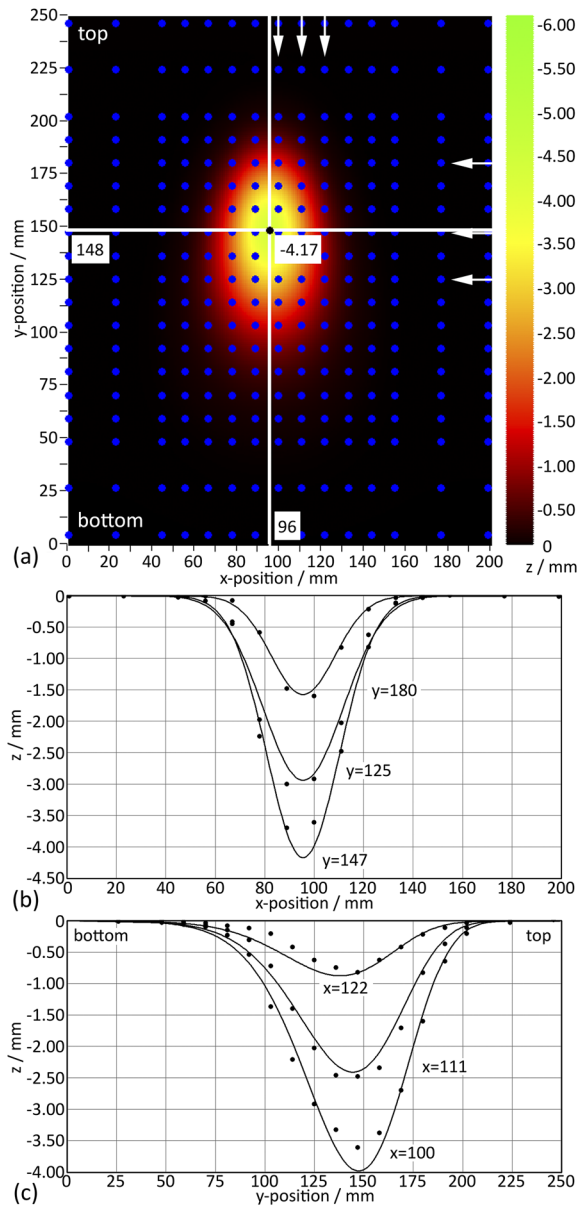
FIG. 3. Approximation of the erosion zone of the Si target at $T = 135,092$ s as also shown in Figs. 2(a) and 2(b). (a) 2D distribution $z_{APPROX}(x,y)$. The 285 positions (x_i, y_i) of the measured erosion depths z_i are marked with blue dots. The fitting parameters are listed in Table II, and the characteristic values are summarized in Table III (line 7). (b) 1D distributions $z_{APPROX}(x, y_i)$ in the x-direction at y_i-positions 125, 147, and 180. (c) 1D distributions $z_{APPROX}(x_i, y)$ in the y-direction at x_i-positions 100, 111, and 122. The arrows in (a) are corresponding to the coordinates of interest in (b) and (c). The data points illustrate the experimentally determined erosion depths z_i.

conditions as described above. On the other hand, the transition between the smooth and rough segments may indicate different levels of target poisoning. With Ta, these effects are not visually recognizable (Fig. 7 in the Appendix).

Outside of the main erosion zone, a wider region of interaction between the charged particle beam and the target can be observed. This region visually extends to the edge, which is marked No. 4 in Fig. 2(a), but even at values $z_{min} \leq -6$ mm, no erosion can be measured with the applied profilometer in this area. Thus, the wide interaction region manifests itself only as a discoloration of the target surface, and it is assumed to result from particles scattered during beam propagation due to a finite mean free path. Besides potential compound formation, additional oxide coverage may occur in the form of an undesired coating when the neighboring target is sputtered. The colored rings at the edge of this wider region indicate dielectric layers with varying layer thicknesses.

Although the Si target was initially fractured (by a handling mistake), it was decided that it should be used anyway for the present investigation. It is conspicuous that the fracture evolved into a mound with a rough side [marked No. 2 in Fig. 2(c)] and a smooth side [marked No. 3 in Fig. 2(c)] during sputtering, most probably as a result of simultaneous redeposition and ion-induced surface modification under varying conditions. No effect of the fracture on the process parameters or quality parameters of the produced films was observed, so the fracture is ignored in the following analyses.

III. EROSION PROFILE APPROXIMATION

For the precise estimation of the characteristics of an erosion profile, each discrete data record $z_i(x_i, y_i)$ is approximated using the following empirical function:

$$z_{APPROX}(x, y) = -z_B(y) \cdot (z_A(y) + z_0 \cdot G(x, y) \cdot H(y)),$$

$$G(x, y) = exp\left\{ -\frac{(x - x_0)^2}{2w(y)^2} \right\},$$

$$H(y) = exp\left\{ -\frac{[ln(y - y_1) - v_2]^2}{2v_1^2} \right\}, \qquad (1)$$

$$z_A(y) = z_1 + z_2 \cdot (y - z_3)^2,$$

$$z_B(y) = z_4 + z_5 \cdot exp\{-z_6 \cdot y\}.$$

$$w(y) = w_1 + w_2 \cdot (y - w_3)^2$$

The above equation was developed starting from the function $R(x, y)$ presented in Ref. 20. Except for the factor $-z_B(y)$, the equations of $z_{APPROX}(x, y)$ and $R(x, y)$ are identical. The minus sign in Eq. (1) indicates an erosion process (removal of particles) instead of a coating process (accumulation of particles). A mirror symmetry for the x-direction is imposed because of $G(x, y)$. More details on the parameters in Eq. (1) are given in Ref. 20. In total, 14 fitting parameters are included in the 2D function $z_{APPROX}(x, y)$ without a direct link to a physical model or the beam profile. As a comparison, for the approximation of a rotationally symmetric erosion zone in a planar magnetron, a one-dimensional (1D) function with six fitting parameters was suggested in Ref. 32. The fitting of $z_{APPROX}(x, y)$ to a determined dataset of erosion depths $z_i(x_i, y_i)$ is performed by the software package Layer-Thickness-Optimization (LTO, developed by Wjatscheslaw Sakiew). The fitting parameters and the corresponding mean squared errors (MSEs) are summarized in Table II.

As a result of the fitting procedure, the following characteristic values of an approximated 2D erosion profile $z_{APPROX}(x, y)$ are

TABLE I. Estimated coordinates of the intersection y_S between the target plane and the lengthened beam vector $\vec{n}_{beam}$. The coordinate system is illustrated in Fig. 2(a).

	y_S (mm)
Ta and Si targets, d_{target} = 370 mm	138 ± 9
SiO$_2$ target, d_{target} = 550 mm	152 ± 12

calculated in LTO: x_0 and y_0 (the coordinates of the maximum erosion depth), $z_{min} \le 0$ (the maximum erosion depth), Δx_{FWHM} and Δy_{FWHM} (the full width at half maximum (FWHM) in the x-direction at the y-position y_0 and in the y-direction at the x-position x_0), and V (the eroded volume). Another advantage of the approximation is the averaging of sporadic erosion depth measurement errors.

In the present work, the erosion profiles are qualitatively compared with one another. For this purpose, the profiles approximated by Eq. (1) are normalized by z_{min} as

$$\overline{z_{APPROX}}(x,y) = z_{APPROX}(x,y)/z_{min}. \qquad (2)$$

Figure 3 shows the approximated sputter-eroded Si target after an erosion time of $T = 135,092$ s. The 1D distributions $z_{APPROX}(x,y_i)$ in the x-direction [Fig. 3(b)] and $z_{APPROX}(x_i,y)$ in the y-direction [Fig. 3(c)] indicate that the accuracy of the approximation for the x-direction is higher than that for the y-direction. It is important to point out that the erosion profile appears symmetrical in the x-direction and asymmetrical in the y-direction as a consequence of the target tilt angle TTA > 0. More precisely, under the conditions considered, the profile is stretched toward the lower target edge (bottom) and squeezed toward the upper target edge (top).

It can be seen that, in Fig. 3, the position of maximum erosion in the x-direction is x_0 = 96 mm, which is not exactly the target center at x = 100 mm. The observed misalignment results from the chosen target holder position and can, therefore, be compensated for by defining a new target holder position. Thus, in the following, the selected erosion profiles are shifted numerically in the x-direction to the target center (x_0 = 100 mm) for a clearer illustration.

In this context, the y-direction is more significant for the present investigation. In Fig. 3, the position of maximum erosion in the y-direction is at y_0 = 148 mm. By measuring the orientation of the target relative to the ion source, the coordinate of the intersection y_S of the beam vector ($\vec{n}_{beam}$ lengthened) with the target surface could not be estimated with better accuracy than shown in Table I, if the manufacturing tolerances of the vacuum chamber and its warping due to high vacuum are taken into account. It is important to note that y_0 and y_S are not necessarily identical.

IV. RESULTS AND DISCUSSION

A. Comparison of the Ta and Si erosion profiles

In Fig. 4, $\overline{z_{APPROX}}(x,y)$ for the Si and Ta targets are compared for identical process geometries (TTA = 55°, d_{target} = 370 mm). Although (1) different materials were eroded with (2) different ion energies and (3) different accumulated erosion times, resulting in (4) different erosion depths z_{min}, and (5) in the case of Ta, both Ar and Xe ions have been used, the determined normalized erosion profiles are almost identical (see also Table III):
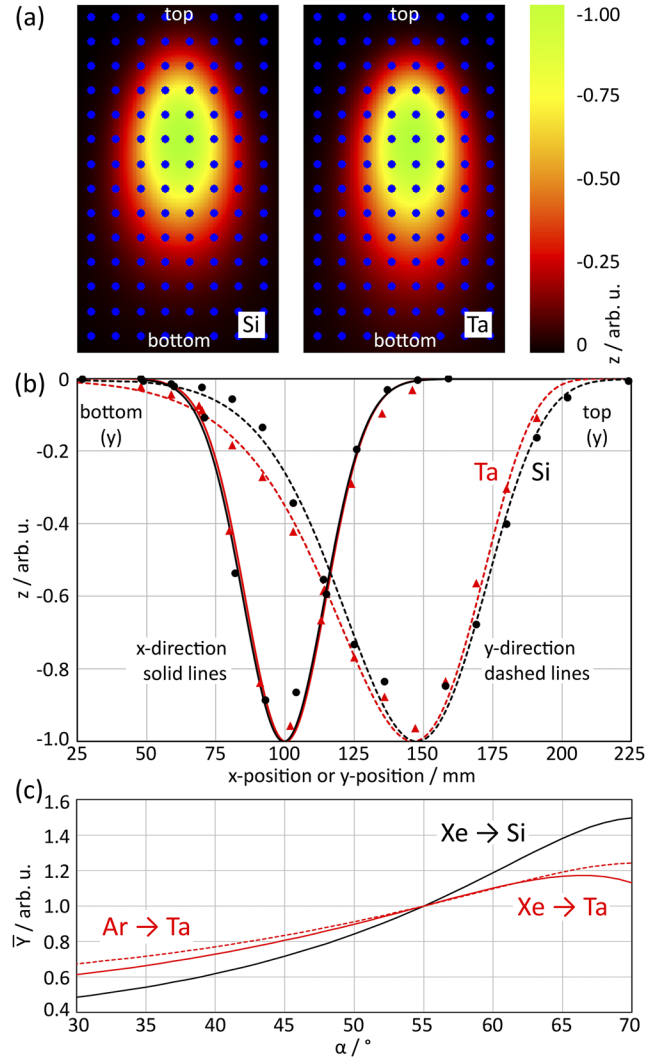

FIG. 4. Si and Ta erosion profiles normalized and represented as in Fig. 3. (a) Two 2D distributions $\overline{z_{APPROX}}(x,y)$. A section of the target area of size 200 × 250 mm^2 is shown. The fitting parameters are listed in Table II, and the characteristic values are summarized in Table III (lines 1 and 7). (b) The 1D distributions of $\overline{z_{APPROX}}(x,147)$ are shown as solid lines and $\overline{z_{APPROX}}(100,y)$ as dashed lines with Si in black and Ta in red. x_0 is centered at x_0 = 100 mm in both cases as described in Sec. III. The coordinates y_0 are within or almost within the range y_S = 138 ± 9 mm given in Table I. (c) Sputtering yields normalized to $\alpha = 55°$ (identical to the applied TTA) as a function of the angle of incidence α onto the target according to the revised Bohdansky model[33] and Yamamura model[34] with $Y(1.4\,\text{keV}\,Xe, Si, \alpha)$ as the black solid line, $Y(1.45\,\text{keV}\,Xe, Ta, \alpha)$ as the red solid line, and $Y(1.8\,\text{keV}\,Ar, Ta, \alpha)$ as the red dashed line.

Positions: It can be seen that the values x_0 and y_0 are almost identical.

Dimensions: The erosion profiles appear identical in the x-direction (the values of Δx_{FWHM} are identical) and similar in the y-direction (the values of Δy_{FWHM} are almost identical).

Stretching: The asymmetrical shapes of the erosion profiles in the y-direction are comparable for the two materials.

The following explanatory approach is plausible: (1) The erosion profiles are mainly influenced by the process geometry (e.g., a rotationally symmetric broad ion beam, a flat and tilted target, the beamlet pattern, and the values of TTA, d_{target}, R_{optic}, and D_{optic}), and (2) the considered ion–solid interaction processes must be assumed to be qualitatively comparable—this means that the normalized sputtering yields, $\overline{Y(\alpha)}$, are similar in the corresponding angular range of ions impinging on the target surface.

Calculations using semi-empirical models[33,34] result in at least similar distributions $\overline{Y(\alpha)}$ (normalized to $\alpha = 55°$) for the sputtering of Ta with Ar ions and Xe ions depending on the angle of incidence of the ions α onto the target [Fig. 4(c)]. The angular dependence of the sputtering of Si compared to Ta appears to deviate more strongly. The variation of the polar angles of incidence along the y-direction is larger than that along the x-direction for the present process geometry, which probably causes the erosion profiles of Ta and Si to differ more in the y-direction than in the x-direction. However, regarding the calculations with the semi-empirical models, it should be noted that, in Ref. 35, it is indicated that the calculation of Y is accurate to within ±20%.

The results in Fig. 4 allow for two further conclusions: (1) If compound formation[17–20] or undesired oxide coverage occurs (Sec. II), then it can only have a minor influence on the qualitative characteristics of the erosion profiles under the experimental boundary conditions presented herein. In particular, because different target materials are compared, different compound formation rates can also be assumed. However, it is quite conceivable that there is a quantitative effect on the erosion rate (a continuous adsorption of oxygen atoms, which then have to be additionally sputtered), which is not evaluated here. (2) If the regulation of the ion energy results in a variation of the beam profile, then this variation must be sufficiently small so that the widths Δx_{FWHM} are not influenced by it. Additionally, the experimentally determined erosion profiles confirm that there is no measurable material removal outside the main erosion zone.

B. Evolution of the Si erosion profile

The investigation of the erosion of the Si target and its dependence on the total accumulated erosion time T can be summarized as follows (see Fig. 5 and Table III):

Positions: There is no significant variation of x_0. This means that the direction of propagation $\vec{n}_{beam}$ of the broad ion beam has not drifted within the observation period (e.g., due to degradation of the ion optic). A small increase in y_0 was documented. This is plausible because the target is tilted relative to $\vec{n}_{beam}$.

Dimensions: Δx_{FWHM} and Δy_{FWHM} increase slightly with increasing T (and increasing z_{min}). However, the variation of both values is 6% or less at a relative erosion depth of approximately 70% ($z_{min}/6$, in comparison with the maximum usable target thickness). Thus, the shape of the erosion profile appears to be almost independent of the erosion time and erosion depth. A similar observation was also documented for DC-MS.[36,37]

Rates: A linear scaling could be identified for z_{min} [Fig. 5(b)] and V [Fig. 5(c)]. The following conclusions can be drawn from this: The erosion rate is constant regardless of the erosion time
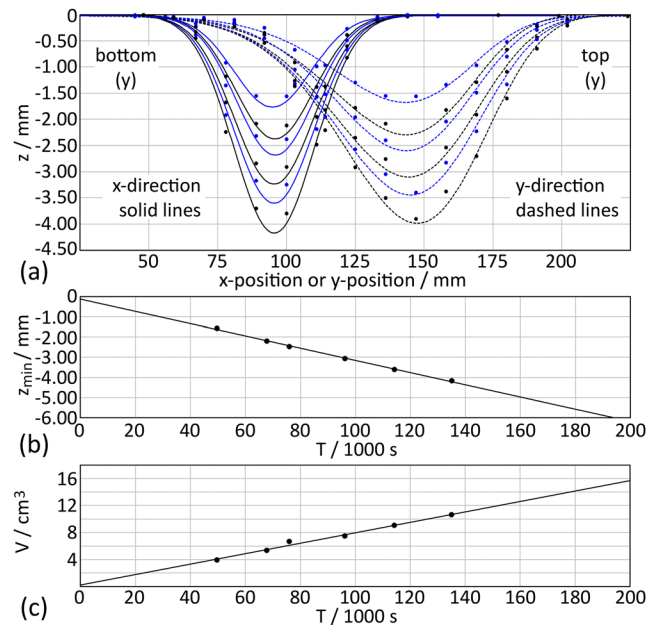
FIG. 5. (a) Evolution of the Si erosion profile as shown in Figs. 2–4. The 1D distributions of $\overline{z_{APPROX}}(x, 147)$ are shown as solid lines and $\overline{z_{APPROX}}(100, y)$ as dashed lines. The circle-shaped points represent the experimentally determined erosion depths z_i. In Table III (lines 2–7), the characteristic values of the approximated erosion profiles are summarized. (b) Maximum erosion depth z_{min} linearly interpolated as a function of T with $z_{min}(T) = -3.024 \cdot 10^{-5} \cdot mm \cdot s^{-1} \cdot T - 0.1342$ mm. Extrapolation to $T = 0$ gives almost 0. According to the interpolation, a target plate thickness of 6 mm is reached after $T = 193,974$ s (~ 54 h). (c) Eroded volume V linearly interpolated as a function of T with $V(T) = 7.706 \cdot 10^{-5}$ cm^3 s^{-1} $T + 0.2602$ cm^3.

or erosion depth. Such a finding is consistent with what is known for MS.[37] It is plausible that the investigated erosion depths are much smaller than the lateral dimensions of a target plate and the broad erosion profile itself. Nevertheless, a clear macroscopic modification of the surface geometry is evident. Consequently, there is also a certain effect on the distribution of the angles of incidence of the ions onto the target surface. However, this effect seems to be sufficiently small such that the change in the angle-dependent sputtering yield (for each ion) during the sputtering of the target is not reflected in the erosion rate [for clarification, see Fig. 4(c)]. This explanation also implies that, for hypothetical erosion depths, which are most probably greater than the thicknesses of the target plates used, non-linearities in the erosion rate must occur. Furthermore, other effects become relevant at large erosion depths, such as the redeposition of the sputtered material. A critical erosion depth cannot be determined at this point, but it is plausible that the critical erosion depth must be smaller than the lateral dimensions of a profile.

If other influences on the erosion rate occur (for the erosion depths investigated), such as compound formation,[17–20] redeposition,[38] target surface composition modification,[39] or ion-induced

surface modifications on the micrometer or nanometer scale (roughening, smoothing, nanopattern formation),[40] then they do not affect the linearity in the performed experiment.

With the observed linearity [Fig. 5(b)], z_{min} can be extrapolated: z_{min} reaches a value of 6 mm (the thickness of the Si target plate) at $T \approx 54$ h (under the conditions of 1.4 keV Xe ions, $I_{beam} = 200$ mA, $d_{target} = 370$ mm). At this point, 5% of the target plate has been eroded. In a production process, however, the position of the target holder can be varied. Thus, from practical experience, depending on the target material, d_{target}, and other ion beam parameters, a target material utilization of up to 20% can be achieved in IBSD before the thickness of a target plate is exceeded. It should be noted that the target size and d_{target}, as applied for present investigation, are optimized for the production of optical coatings with the highest quality level. Through additional technical adaptations (e.g., target segmentation), a higher degree of utilization can be achieved.

C. Comparison of the erosion profiles at different distances d_{target}

In Fig. 4, it is shown that the erosion profiles of Ta and Si are qualitatively almost identical if the target distance d_{target} is not changed, despite the different materials. On the basis of this result (process geometry appears superordinate, ion–solid interaction mechanisms appear subordinate), the dielectric SiO$_2$ target was eroded at a distance 180 mm larger. On the one hand, the greater propagation length of the broad ion beam through the process atmosphere and the associated interaction mechanisms that influence the characteristics of the ion beam should be taken into account. On the other hand, it should be considered that the SiO$_2$ target was positioned clearly behind the geometric focal point of the ion optic ($d_{target} > R_{optic}$), while the other two targets were positioned close to but still in front of the geometric focal point ($d_{target} < R_{optic}$). The following results were obtained (see Fig. 6 and Table III):

Positions: The coordinate y_0 of the maximum erosion depth z_{min} is smaller. More precisely, y_0 shifts below the coordinate y_S (Table I). It is assumed that this behavior results from the photometric law and the corresponding beam profile.

Dimensions: The erosion profile becomes broader. Δx_{FWHM} and Δy_{FWHM} scale with an almost identical scaling factor of 1.6 by increasing d_{target} from 370 to 550 mm, although different target materials are being compared at this point. This result can also be understood as an indication that the erosion profiles are more strongly influenced by geometrical parameters than by ion–solid interaction mechanisms, as mentioned in Sec. IV A.

Stretching: Compared to the Ta and Si erosion profiles, the qualitative characteristic of the SiO$_2$ erosion profile along the y-direction is reversed at the larger distance. The profile is stretched toward the upper target edge (top) and squeezed toward the lower target edge (bottom).

It can be concluded that, in qualitative terms, the erosion depends significantly on the propagation length of the broad ion beam or the characteristics of the ion beam. An uncertainty in the
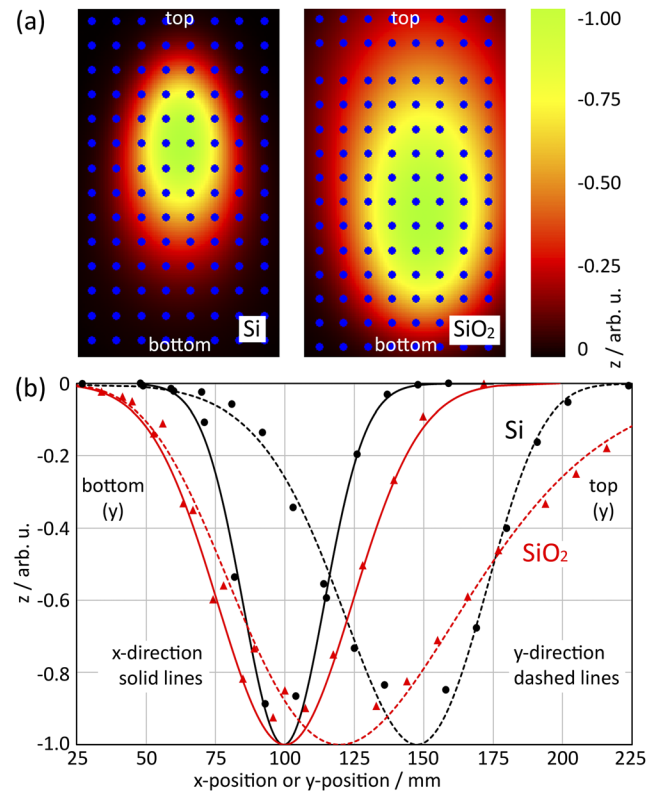

FIG. 6. Si and SiO$_2$ erosion profiles normalized and represented as in Fig. 3. $d_{target} = 370$ mm in the case of Si, and $d_{target} = 550$ mm in the case of SiO$_2$. (a) Two 2D distributions $\overline{z_{APPROX}}(x, y)$. A section of the target area of size 200 × 250 mm^2 is shown. The fitting parameters are listed in Table II, and the characteristic values are summarized in Table III (lines 2 and 8). (b) 1D distributions for Si are shown in black and are identical to those in Fig. 4(b). The 1D distributions $\overline{z_{APPROX}}(x, 120)$ are shown as solid lines and $\overline{z_{APPROX}}(100, y)$ as dashed lines with SiO$_2$ in red. $x_0 = 100$ mm in both cases as described in Sec. III. In the case of SiO$_2$, $y_0 = 120$ mm is clearly out of the range $y_S = 152 \pm 12$ mm given in Table I. The triangle-shaped points represent the experimentally determined erosion depths z_i. They are assigned to the coordinates $x_i = 100$ mm and $y_i = 122$ mm as the closest coordinates to $x_0 = 100$ mm and $y_0 = 120$ mm.

result arises from the fact that metallic and dielectric targets are being compared at this point. In the case of SiO$_2$, charging effects are conceivable, as well as preferential sputtering.[41]

V. SUMMARY AND CONCLUSIONS

The focus of this work was to investigate target erosion profiles during low-energy (ion energy ≤1.9 keV, ion source RIM-20) reactive broad ion beam sputtering on a millimeter scale. Erosion profiles sputter-eroded from flat Ta, Si, and SiO$_2$ targets were compared with one another. For the precise estimation of the characteristics of an erosion profile, an empirical approximation function was developed.

The experimental data showed similar erosion profiles when comparing Ta (sputtered by 1.8 keV Ar and 1.45 keV Xe ions) and

Si (sputtered by 1.4 keV Xe ions). In the case of Si, a linear erosion rate as a function of erosion time was observed. The qualitative distribution of the Si erosion profile appeared to be almost independent of the erosion time and erosion depth. Furthermore, a comparison of Si and SiO_2 (sputtered by 1.9 keV Ar ions) target erosion profiles, with the targets being eroded at different distances from the ion optic, showed a clear dependence on the propagation length of the broad ion beam. The lateral dimensions of the erosion profile and the position of the maximum erosion depth both changed. Furthermore, the shape of the profile along the y-direction was completely reversed. This behavior is associated with the beam profile and the photometric law.

The experimental results allow for the conclusion that the qualitative characteristics of the erosion profiles on a macroscopic scale are more strongly coupled to geometrical parameters (e.g., a rotationally symmetric broad ion beam, a flat and tilted target, the distance between the ion optic and the target, and the ion optic radius of curvature and diameter) than to the considered ion–solid interaction mechanisms at an atomic level, which are particularly coupled to the ion species and ion energy. It is conceivable that this result can be transferred to other broad ion beam sources commonly used in IBSD if a similar experimental setup is considered.

The impact of potential compound formation on the meaning of Berg's model, which is hardly accessible experimentally, is unclear. In particular, for modeling of the target erosion in IBS, target poisoning is still a challenge.

ACKNOWLEDGMENTS

APPENDIX: TABLES AND FIGURES

Table II lists the fitting parameters of the approximated erosion profiles $z_{APPROX}(x, y)$; Table III lists the characteristic values of the approximated erosion profiles $z_{APPROX}(x, y)$; and Fig. 7 shows the top view of a sputter-eroded Ta target with dimensions $200 \times 250 \times 6$ mm^3, sputtered with different ion beam parameters as described in Sec. II.

TABLE II. Fitting parameters of the approximated erosion profiles $z_{APPROX}(x, y)$. The erosion profiles of Ta and Si must be rotated numerically by 180°. The fitting of $z_{APPROX}(x, y)$ to a determined dataset of erosion depths $z_i(x_i, y_i)$ is performed by the software package LTO. The total number of data points is 150 for Ta, 285 for Si, and 315 for SiO_2. In column 2, the corresponding mean squared error (MSE) is given.

Target (figure)	MSE	Fitting parameters
Ta (Fig. 4)	$2.7 \cdot 10^{-2}$	$x_0 = 101.820$, $y_1 = -0.039$, $z_0 = 9.433$, $z_1 = 1.0 \cdot 10^{-4}$, $z_2 = 1.553 \cdot 10^{-9}$, $z_3 = -6.562 \cdot 10^{-4}$, $z_4 = 0.036$, $z_5 = 0.241$, $z_6 = 0.013$, $v_1 = 0.258$, $v_2 = 4.698$, $w_1 = 10.870$, $w_2 = 3.461 \cdot 10^{-4}$, $w_3 = -0.047$
Si (Figs. 3–6)	$5.1 \cdot 10^{-1}$	$x_0 = 104.468$, $y_1 = -63.865$, $z_0 = 28.823$, $z_1 = 0.019$, $z_2 = 1.049 \cdot 10^{-6}$, $z_3 = -4.065 \cdot 10^{-3}$, $z_4 = -0.021$, $z_5 = 0.460$, $z_6 = 9.640 \cdot 10^{-3}$, $v_1 = 0.158$, $v_2 = 5.158$, $w_1 = 11.373$, $w_2 = 3.131 \cdot 10^{-4}$, $w_3 = -3.683 \cdot 10^{-5}$
SiO_2 (Fig. 6)	$1.7 \cdot 10^{-2}$	$x_0 = 103.548$, $y_1 = -62.109$, $z_0 = 48.452$, $z_1 = 4.297 \cdot 10^{-4}$, $z_2 = -1 \cdot 10^{-8}$, $z_3 = 500$, $z_4 = -4.443 \cdot 10^{-3}$, $z_5 = 0.958$, $z_6 = 1.388 \cdot 10^{-2}$, $v_1 = 0.243$, $v_2 = 5.355$, $w_1 = 22.569$, $w_2 = 3.067 \cdot 10^{-4}$, $w_3 = 44.887$

TABLE III. Characteristic values of the approximated erosion profiles $z_{APPROX}(x, y)$ as described in Sec. III. All calculations are performed with LTO.

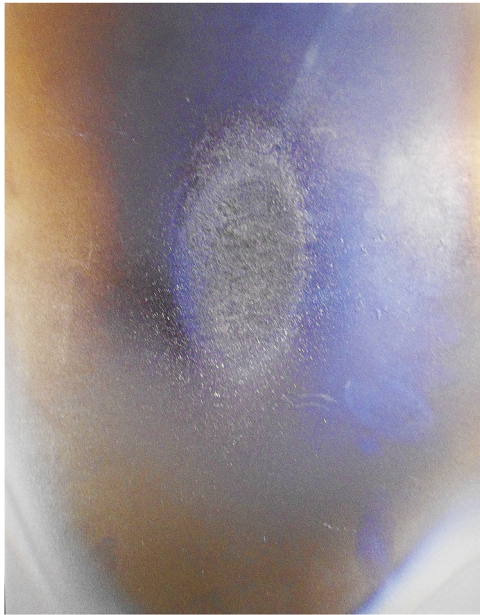| Target (figure)	T (s)	x_0 (mm)	y_0 (mm)	z_{min} (mm)	Δx_{FWHM} (mm)	Δy_{FWHM} (mm)	V (mm^3)
Ta (Fig. 4)	...	98	146	−0.93	35.0	64.0	2 505
Si (Fig. 5)	49 756	95	142	−1.58	33.0	59.0	3 925
Si (Fig. 5)	67 869	96	143	−2.20	33.5	59.0	5 358
Si (Fig. 5)	76 058	96	143	−2.48	33.5	58.5	6 639
Si (Fig. 5)	96 215	95	144	−3.07	34.5	60.5	7 492
Si (Fig. 5)	114 178	95	146	−3.61	34.5	61.0	9 050
Si (Fig. 5)	135 092	96	148	−4.17	35.0	61.0	10 644
SiO_2 (Fig. 6)	...	104	120	−7.06	57.0	97.0	46 309

FIG. 7. Top view of a sputter-eroded Ta target with dimensions $200 \times 250 \times 6$ mm^3, sputtered with different ion beam parameters as described in Sec. II. The fitting parameters of the corresponding approximated erosion profile are listed in Table II, and the resulting characteristic values are summarized in Table III.

DATA AVAILABILITY

The data that support the findings of this study are available within this article.

REFERENCES

[1]D. Ristau and T. Gross, in *Advances in Optical Thin Films II*, edited by C. Amra, N. Kaiser, and H. A. Macleod (SPIE, 2005), Vol. 5963, p. 596313.

[2]C. J. Stolz and R. A. Negres, Opt. Eng. **57**, 1 (2018).

[3]M. Becker, M. Gies, A. Polity, S. Chatterjee, and P. J. Klar, Rev. Sci. Instrum. **90**, 023901 (2019).

[4]J. Degallaix, C. Michel, B. Sassolas, A. Allocca, G. Cagnoli, L. Balzarini, V. Dolique, R. Flaminio, D. Forest, M. Granata, B. Lagrange, N. Straniero, J. Teillon, and L. Pinard, J. Opt. Soc. Am. A **36**, C85 (2019).

[5]J. Belfi, N. Beverini, F. Bosi, G. Carelli, D. Cuccato, G. De Luca, A. Di Virgilio, A. Gebauer, E. Maccioni, A. Ortolan, A. Porzio, G. Saccorotti, A. Simonelli, and G. Terreni, Rev. Sci. Instrum. **88**, 034502 (2017).

[6]H. Ehlers and D. Ristau, in *Optical Thin Films and Coatings*, 2nd ed., edited by A. Piegari and F. Flory (Woodhead Publishing, 2018), pp. 103–140.

[7]M. Jupé, M. Lappschies, L. Jensen, K. Starke, and D. Ristau, in *Proceedings Vol. 6403, Laser-Induced Damage Optical Materials 2006*, edited by G. J. Exarhos, A. H. Guenther, K. L. Lewis, D. Ristau, M. J. Soileau, and C. J. Stolz (SPIE, 2007), p. 640311.

[8]T. Willemsen, M. Jupé, L. Gallais, D. Tetzlaff, and D. Ristau, Opt. Lett. **42**, 4502 (2017).

[9]S. Malobabic, M. Jupé, and D. Ristau, Light: Sci. Appl. **5**, e16044 (2016).

[10]C. Bundesmann and H. Neumann, J. Appl. Phys. **124**, 231102 (2018).

[11]H. Badorreck, M. Steinecke, L. Jensen, D. Ristau, M. Jupé, J. Müller, R. Tonneau, P. Moskovkin, S. Lucas, A. Pflug, L. Grinevičiūtė, A. Selskis, and T. Tolenis, Opt. Express **27**, 22209 (2019).

[12]W. Sakiew, S. Schrameyer, P. Schwerdtner, N. Erhart, and K. Starke, Appl. Opt. **59**, 4296 (2020).

[13]A. Ribeaud, J. Pistner, H. Hagedorn, M. Brophy, P. Kupinski, J. Watson, and R. Hand, in *Laser-Induced Damage Optical Materials 2018 50th Anniversary Conference*, edited by C. W. Carr, G. J. Exarhos, V. E. Gruzdev, D. Ristau, and M. J. Soileau (SPIE, 2018), pp. 134–142.

[14]T. A. Laurence, D. A. Alessi, E. Feigenbaum, R. A. Negres, S. R. Qiu, C. W. Siders, T. M. Spinka, and C. J. Stolz, J. Appl. Phys. **128**, 071101 (2020).

[15]M. Becker, X. Li, T. Henning, and P. J. Klar, Rev. Sci. Instrum. **91**, 013905 (2020).

[16]Y. Chen, D. Hahner, M. Trubetskov, S. Schrameyer, W. Sakiew, K. Starke, and V. Pervak, Appl. Phys. B **126**, 82 (2020).

[17]S. Berg, E. Särhammar, and T. Nyberg, Thin Solid Films **565**, 186 (2014).

[18]K. Strijckmans and D. Depla, J. Phys. D: Appl. Phys. **47**, 235302 (2014).

[19]T. Lautenschläger, *Systematic Investigation of the Ion Beam Sputter Deposition of TiO$_2$* (Universität Leipzig, 2018).

[20]W. Sakiew, S. Schrameyer, M. Jupé, P. Schwerdtner, N. Erhart, K. Starke, and D. Ristau, Thin Solid Films **682**, 109 (2019).

[21]M. Sangregorio, K. Xie, N. Wang, N. Guo, and Z. Zhang, Chin. J. Aeronaut. **31**, 1635 (2018).

[22]Y. Lu, X. Xie, L. Zhou, Z. Dai, and G. Chen, Appl. Opt. **56**, 260 (2017).

[23]J. Bauer, F. Frost, and T. Arnold, J. Phys. D: Appl. Phys. **50**, 085101 (2017).

[24]T. Arnold, G. Böhm, R. Fechner, J. Meister, A. Nickel, F. Frost, T. Hänsel, and A. Schindler, Nucl. Instrum Methods Phys. Res., Sect. A **616**, 147 (2010).

[25]T. Amelal, L. Pietzonka, E. Rohkamm, and C. Bundesmann, J. Vac. Sci. Technol., A **38**, 033403 (2020).

[26]K. Oh, D. Kalanov, A. Anders, and C. Bundesmann, J. Vac. Sci. Technol., A **38**, 033011 (2020).

[27]D. Kalanov, A. Anders, and C. Bundesmann, J. Vac. Sci. Technol., A **37**, 051507 (2019).

[28]T. Lautenschläger and C. Bundesmann, J. Vac. Sci. Technol., A **35**, 041001 (2017).

[29]H. W. Loeb, in *AIAA 7th Electric Propulsion Conference* (AIAA, Williamsburg, Virginia, 1969), p. 285.

[30]J. Freisinger, J. Heland, D. Krämer, H. Löb, and A. Scharmann, Rev. Sci. Instrum. **63**, 2571 (1992).

[31]M. Zeuner, F. Scholze, H. J. Leiter, R. Kukies, D. Feili, M. Tartz, and H. Neumann, in *39th AIAA/ASME/SAE/ASEE Joint Propulsion Conference Exhibition* (AIAA, 2003), p. 5009.

[32]A. V. Rogov and Y. V. Kapustin, Tech. Phys. **62**, 1437 (2017).

[33]C. García-Rosales, W. Eckstein, and J. Roth, J. Nucl. Mater. **218**, 8 (1995).

[34]Y. Yamamura, Y. Itikawa, and N. Itoh, *Angular Dependence of Sputtering Yields of Monoatomic Solids* (Institute of Plasma Physics, Nagoya University, 1983).

[35]N. Matsunami, Y. Yamamura, Y. Itikawa, N. Itoh, Y. Kazumata, S. Miyagawa, K. Morita, R. Shimizu, and H. Tawara, At. Data Nucl. Data Tables **31**, 1 (1984).

[36]D. Depla, K. Strijckmans, and R. De Gryse, Surf. Coat. Technol. **258**, 1011 (2014).

[37]T. Nakano, Y. Saitou, and K. Oya, Surf. Coat. Technol. **326**, 436 (2017).

[38]N. Anspach and S. J. Linz, J. Stat. Mech. Theory Exp. **2010**, P06023.

[39]C. Bundesmann, T. Lautenschläger, D. Spemann, A. Finzel, E. Thelander, M. Mensing, and F. Frost, Appl. Surf. Sci. **421**, 331 (2017).

[40]F. Frost, B. Ziberi, A. Schindler, and B. Rauschenbach, Appl. Phys. A **91**, 551 (2008).

[41]M. Mende, F. Carstens, H. Ehlers, and D. Ristau, J. Vac. Sci. Technol., A **39**, 023406 (2021).